MITSUBISHI ELECTRIC RESEARCH LABORATORIES
https://www.merl.com

A model of spatial resolution uncertainty for Compton camera imaging

Ma, Yanting; Rapp, Joshua; Boufounos, Petros T.; Mansour, Hassan

TR2024-005 January 17, 2024

Abstract

Compton cameras use a pair of detectors to record the energy deposited during Compton scattering and photoabsorption of gamma ray photons. By inverting the forward model for these detection events, the 3D radioactive source distribution can be recovered computationally. However, existing methods of describing the forward model ignore the ambiguity in the Compton cone axis introduced by the detector pixel size. In this paper, we introduce approximations to the axis ambiguity that make the description of the source ambiguity computationally tractable and improve the accuracy of the detection forward model. Specifically, we model the pixel active areas as discs, so the intersection between all possible Compton cone axes and a plane parallel to the detectors is also a disc. Because of ambiguity in the Compton cone axis, the gamma source position is constrained to lie within a more complicated volume that we approximately bound by ellipses or hyperbolas at discrete depth slices. We perform simulations of single point gamma sources using the Geant4 software. Our forward model leads to improved source distribution recovery using both backprojection and iterative reconstruction methods, demonstrating that accurate localization can be performed from a smaller number of detected photons.

International Conference on Advancements in Nuclear Instrumentation Measurement Methods and their Applications (ANIMMA) 2024

Mitsubishi Electric Research Laboratories, Inc.
201 Broadway, Cambridge, Massachusetts 02139

A model of spatial resolution uncertainty for Compton camera imaging

Yanting Ma, Joshua Rapp, Petros Boufounos, Hassan Mansour
Mitsubishi Electric Research Laboratories (MERL), USA
yma@merl.com

***Abstract*—Compton cameras use a pair of detectors to record the energy deposited during Compton scattering and photoabsorption of gamma ray photons. By inverting the forward model for these detection events, the 3D radioactive source distribution can be recovered computationally. However, existing methods of describing the forward model ignore the ambiguity in the Compton cone axis introduced by the detector pixel size. In this paper, we introduce approximations to the axis ambiguity that make the description of the source ambiguity computationally tractable and improve the accuracy of the detection forward model. Specifically, we model the pixel active areas as discs, so the intersection between all possible Compton cone axes and a plane parallel to the detectors is also a disc. Because of ambiguity in the Compton cone axis, the gamma source position is constrained to lie within a more complicated volume that we approximately bound by ellipses or hyperbolas at discrete depth slices. We perform simulations of single point gamma sources using the Geant4 software. Our forward model leads to improved source distribution recovery using both backprojection and iterative reconstruction methods, demonstrating that accurate localization can be performed from a smaller number of detected photons.**

***Keywords*—Compton camera, list-mode maximum likelihood, spatial resolution, source localization**

I. Introduction

Compton scattering of high-energy photons, such as gamma rays, can be modelled as an inelastic collision, transferring energy and momentum to a single electron [1]. This phenomenon is used in so-called "Compton cameras" to measure the location and angle of arrival of gamma photons. Constructed from two or more radiation-sensitive layers, these imagers detect and record the location and deposited energy of high-energy photons, which theoretically constrains the gamma source to lie on the surface of a cone. Compton cameras have largely been used for astronomy and medical imaging, although an important growing application area is localization of nuclear waste, both within power plants and externally, e.g., as a result of the Fukushima Daiichi accident.

Initial approaches to Compton imaging were influenced by astronomical applications and were predominantly focused on two-dimensional (2D) reconstructions [2], [3]. Recent work has aimed to solve the more challenging tomography problem of reconstructing the 3D distribution of radioactive sources [4], [5], [6], [7], [8], [9]. A fundamental hurdle in Compton tomography is accurately constructing the measurement matrix, namely accounting for the uncertainty in the Compton cone based on ambiguity in the detector. As identified in early works, the main sources of ambiguity are the energy resolution, spatial resolution, and thickness of the detectors, and the distance of the radioactive source to the imager [10]. Research efforts have begun to tackle a number of these issues, including the photon's incident angle [11], [4], [5], the finite extent of the detector [6], and the detector's energy resolution [7].

Compton imaging in nuclear medicine requires only short-range measurements and can use high-resolution silicon strip detectors, so ambiguity due to detector spatial resolution is low and has been specifically neglected (e.g., in [7]). The Compton cone axis is thus assumed to be known exactly, leading to the intersection of the Compton cone with a plane at a fixed depth from the camera to be idealized as an ellipse. However, applications such as robotic radiation source localization (e.g., [12]) require lower-resolution scintillator-based detectors that are more rugged, lower cost, more efficient, and larger area [13]. Significant uncertainty in accurately determining the axis of the Compton cone is incurred due to the larger scintillator-based detector elements, so instead of being restricted to the surface of a cone, the gamma photon's source location lies in a volume of ambiguity. Furthermore, methods such as [4], which chooses the 3D voxel size based on the detector pixel size, naively assume the 3D position uncertainty is on the order of the detector pixel size, ignoring the increase in ambiguity as a function of distance from the imager.

In this paper, we explicitly model the ambiguity in the cone axis due to the detector pixel size. By approximating the active pixel area by a disc, we show instead that at each depth plane, plausible source locations fall in regions approximately bounded by ellipses and hyperbolas. We incorporate the spatial resolution uncertainty to construct an improved measurement matrix, which we use in an iterative reconstruction procedure to show improved source localization from fewer photon detections.

II. Compton imaging model

A. Compton Cone

A classical model of Compton camera detection is depicted in Fig. 1. Ideally, an incoming gamma photon undergoes Compton scattering at the first detector array (scatterer) and is completely absorbed at the second detector array (absorber). We call this pair of interactions (scattering and absorption) an *event*. Let E_γ be the incident photon energy and let $\tilde{E}_\mathrm{s}$ and $\tilde{E}_\mathrm{a}$ be the energy deposited at the scatterer and absorber, respectively. Suppose that the gamma photon hits the scatterer

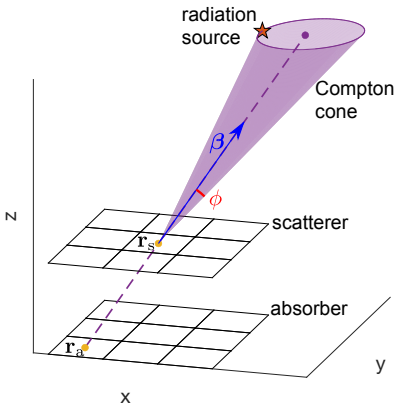

Fig. 1: Measurements of energy deposited at $\mathbf{r}_s$ on the scatterer and $\mathbf{r}_a$ on the absorber restrict the gamma photon source to lie on the Compton cone defined by axis vector $\boldsymbol{\beta}$ and angle ϕ. Coarse detector spatial resolution causes ambiguity in $\boldsymbol{\beta}$.

at position $\tilde{\mathbf{r}}_s$ and absorber at position $\tilde{\mathbf{r}}_a$. Then the position of the incident gamma photon is known to be located on the surface of a cone, where the cone is determined by $(\tilde{\mathbf{r}}_s, \tilde{\mathbf{r}}_a, \tilde{E}_s, \tilde{E}_a)$. Specifically, the vertex is $\tilde{\mathbf{r}}_s$, and the axis vector $\tilde{\boldsymbol{\beta}}$ and the half-angle $\tilde{\phi}$ are defined as

$$\tilde{\boldsymbol{\beta}} = \frac{\tilde{\mathbf{r}}_s - \tilde{\mathbf{r}}_a}{\|\tilde{\mathbf{r}}_s - \tilde{\mathbf{r}}_a\|} \tag{1}$$

$$\cos\tilde{\phi} = 1 - \frac{m_e c^2 \tilde{E}_s}{(\tilde{E}_s + \tilde{E}_a)\tilde{E}_a}, \tag{2}$$

where m_e is the mass of an electron at rest ($m_e c^2 = 0.5510$ MeV).[1]

We observe that the cone angle $\tilde{\phi}$ depends on the detector energies, and the effect of the energy resolution on 3D reconstruction has been investigated previously, e.g., [14]. On the other hand, the cone axis $\tilde{\boldsymbol{\beta}}$ depends on the position of the Compton scattering and photon absorption events. In newer, 3D-position-sensitive detectors (e.g., CdZnTe), energy deposition is measured at a continuum of depths, and a multivariate Gaussian position uncertainty model has been explored in [15]. However, the conventional detectors we consider have fixed detector arrays layers without spatial sensitivity, so measured positions are assigned to be the center of the pixels in which these interactions are detected, which we denote $\mathbf{r}_s$ and $\mathbf{r}_a$. The errors between the assigned and actual event positions ($\|\mathbf{r}_s - \tilde{\mathbf{r}}_s\|$, $\|\mathbf{r}_a - \tilde{\mathbf{r}}_a\|$) depend on the spatial resolution, i.e., the size of the detector pixels. Because $\boldsymbol{\beta}$ is affected by errors in both $\mathbf{r}_s$ and $\mathbf{r}_a$, the cone axis error is magnified as a function of the distance of the radiation source relative to the Compton camera.

B. Forward Model

The radiation source can be described as an intensity distribution $\boldsymbol{\lambda}$ in three spatial dimensions. The goal of the inverse problem is to reconstruct the intensity distribution given the Compton camera measurements. The most important step toward inversion is carefully defining the forward model that describes how gamma rays generate Compton camera measurements.

We first define a computational domain that specifies the extent of the volume in which to reconstruct the intensity distribution and discretizes this volume into voxels. Because of the high dimensionality of the photon coincidence, high-resolution discretization or "binning" of the measurement space leads to an extremely large measurement matrix, and the number of coincidence events is typically low, so most bins would have zero associated events. As a result, we follow the convention of using list-mode data [16], separately storing the measurement 4-tuple $(\mathbf{r}_s, \mathbf{r}_a, E_s, E_a)$ for each event. We can also represent a measurement as a 3-tuple $(\mathbf{r}_s, \mathbf{r}_a, \phi)$, where ϕ is computed from E_s and E_a according to (2).

The system matrix $\mathbf{T}$ relates the source distribution to the measurement space, with element $\mathbf{T}_{i,j}$ defined as the probability that a photon emitted from the j^{th} voxel in the computational domain is measured as the i^{th} event. We also define the sensitivity vector $\mathbf{s}$, where element $\mathbf{s}_j$ is the probability that a photon emitted from the j^{th} voxel is measured by the camera.

1) General Form of the System Matrix: A general form of system matrix has been proposed in [7]. Suppose that the i^{th} event is associated with measurement $(\mathbf{r}_s^{(i)}, \mathbf{r}_a^{(i)}, \phi^{(i)})$, then the $(i,j)^{\text{th}}$ element of the system matrix $\mathbf{T}$ is defined as

$$\begin{aligned}\mathbf{T}_{i,j} = \frac{1}{\text{vol}(V_j)} \int_{V_j} \int_{\mathbb{R}^3} \Bigg\{ & \frac{|\cos[\angle(\mathbf{x} - \tilde{\mathbf{r}}'_s)]|}{\|\mathbf{x} - \tilde{\mathbf{r}}'_s\|_2^2} p_{\mathbf{r}_s|\tilde{\mathbf{r}}_s}(\mathbf{r}_s^{(i)}|\tilde{\mathbf{r}}'_s) \\ & \int_{\mathbb{R}^3} \frac{|\cos[\angle(\tilde{\mathbf{r}}'_a - \tilde{\mathbf{r}}'_s)]|}{\|\tilde{\mathbf{r}}'_a - \tilde{\mathbf{r}}'_s\|_2^2} p_{\mathbf{r}_a|\tilde{\mathbf{r}}_a}(\mathbf{r}_a^{(i)}|\tilde{\mathbf{r}}'_a) \\ & K(\phi(\mathbf{x}; \tilde{\mathbf{r}}'_a, \tilde{\mathbf{r}}'_s)|E_\gamma) \\ & p_{\phi|\tilde{\phi}}\left(\phi^{(i)}|\phi(\mathbf{x}; \tilde{\mathbf{r}}'_a, \tilde{\mathbf{r}}'_s)\right) \Bigg\} \, \mathrm{d}\tilde{\mathbf{r}}'_a \, \mathrm{d}\tilde{\mathbf{r}}'_s \, \mathrm{d}\mathbf{x} \,,\end{aligned} \tag{3}$$

where $K(\phi|E_\gamma)$ is the angular distribution given by the Klein-Nishina formula [17], $V_j \subset \mathbb{R}^3$ is the j^{th} voxel in the computational domain, $\phi(\mathbf{x}; \tilde{\mathbf{r}}'_a, \tilde{\mathbf{r}}'_s)$ is the angle between $\mathbf{x} - \tilde{\mathbf{r}}'_s$ and $\tilde{\mathbf{r}}'_s - \tilde{\mathbf{r}}'_a$, $\angle\mathbf{a}$ is the angle between vector $\mathbf{a}$ and the z-axis, and the conditional probability distributions $p_{\mathbf{r}_s|\tilde{\mathbf{r}}_s}$, $p_{\mathbf{r}_a|\tilde{\mathbf{r}}_a}$, and $p_{\phi|\tilde{\phi}}$ model, respectively, the spatial ambiguity on the scatterer and absorber, and the half-angle ambiguity due to limited energy resolution. According to [7], the sensitivity can be approximated as

$$\mathbf{s}_j = \sum_k \frac{|\cos[\angle(\mathbf{v}_j - \tilde{\mathbf{r}}_s^{(k)})]|}{\|\mathbf{v}_j - \tilde{\mathbf{r}}_s^{(k)}\|_2^2}, \tag{4}$$

where the summation is over all scatterer pixel center positions $\tilde{\mathbf{r}}_s^{(k)}$ and $\mathbf{v}_j$ denotes the center of the voxel V_j. In [7], spatial ambiguity is ignored, i.e., $p_{\mathbf{r}_s|\tilde{\mathbf{r}}_s}(\mathbf{r}_s|\tilde{\mathbf{r}}_s) = \delta(\mathbf{r}_s - \tilde{\mathbf{r}}_s)$ and $p_{\mathbf{r}_a|\tilde{\mathbf{r}}_a}(\mathbf{r}_a|\tilde{\mathbf{r}}_a) = \delta(\mathbf{r}_a - \tilde{\mathbf{r}}_a)$, and the half-angle ambiguity $p_{\phi|\tilde{\phi}}(\phi|\tilde{\phi})$ is modeled as Gaussian with mean $\tilde{\phi}$.

2) Proposed Implementation of Cone Surface Integral: If we assumed no ambiguity in the measurements, then all $p_{\mathbf{r}_s|\tilde{\mathbf{r}}_s}$,

[1] We use letters marked with a tilde to denote the idealized values assuming infinite spatial and energy resolution, whereas letters without tilde will be used to denote the measured value by a practical Compton camera.

$p_{\mathbf{r}_\mathrm{a}|\tilde{\mathbf{r}}_\mathrm{a}}$, and $p_{\phi|\tilde{\phi}}$ are Dirac delta functions, and the forward operator becomes the conventional cone surface model

$$\mathbf{T}_{i,j} = K(\phi^{(i)}|E_\gamma)\frac{|\cos[\angle(\mathbf{r}_\mathrm{a}^{(i)}-\mathbf{r}_\mathrm{s}^{(i)})]|}{\|\mathbf{r}_\mathrm{a}^{(i)}-\mathbf{r}_\mathrm{s}^{(i)}\|_2^2}\frac{1}{\mathrm{vol}(V_j)} \int_{V_j}\frac{|\cos[\angle(\mathbf{x}-\mathbf{r}_\mathrm{s}^{(i)})]|}{\|\mathbf{x}-\mathbf{r}_\mathrm{s}^{(i)}\|_2^2}\delta(\phi^{(i)}-\phi(\mathbf{x};\mathbf{r}_\mathrm{a}^{(i)},\mathbf{r}_\mathrm{s}^{(i)}))\,\mathrm{d}\mathbf{x}\,, \tag{5}$$

which integrates over all points on the cone surface within V_j. Numerous methods have been proposed for computing the cone surface integrals for Compton imaging. Here we propose a convenient approximation, which we use for the baseline comparison that ignores spatial resolution ambiguity.

Assuming sufficiently small voxels, we can approximate the integral in (5) by evaluating based only on the value at the voxel center $\mathbf{v}_j$ and whether the cone surface intersects V_j:

$$\mathbf{T}_{i,j}^{\mathrm{surf}} \propto K(\phi^{(i)}|E_\gamma)\frac{|\cos[\angle(\mathbf{r}_\mathrm{a}^{(i)}-\mathbf{r}_\mathrm{s}^{(i)})]|}{\|\mathbf{r}_\mathrm{a}^{(i)}-\mathbf{r}_\mathrm{s}^{(i)}\|_2^2} \frac{|\cos[\angle(\mathbf{v}_j-\mathbf{r}_\mathrm{s}^{(i)})]|}{\|\mathbf{v}_j-\mathbf{r}_\mathrm{s}^{(i)}\|_2^2}\mathbb{I}_{\mathrm{cone}}(V_j;\mathbf{r}_\mathrm{a}^{(i)},\mathbf{r}_\mathrm{s}^{(i)},\phi^{(i)})), \tag{6}$$

where the indicator function is defined as

$$\mathbb{I}_{\mathrm{cone}}(V_j;\mathbf{r}_\mathrm{a}^{(i)},\mathbf{r}_\mathrm{s}^{(i)},\phi^{(i)})) = \begin{cases} 1, & \text{cone defined by } (\mathbf{r}_\mathrm{a}^{(i)},\mathbf{r}_\mathrm{s}^{(i)},\phi^{(i)}) \text{ intersects } V_j \\ 0, & \text{otherwise.} \end{cases} \tag{7}$$

To determine $\mathbb{I}_{\mathrm{cone}}(V_j)$, we first describe the surface of the cone as the zero-level set of the equation

$$g(\mathbf{x};\mathbf{r}_\mathrm{s},\boldsymbol{\beta},\phi) = \left\langle \frac{\mathbf{x}-\mathbf{r}_\mathrm{s}}{\|\mathbf{x}-\mathbf{r}_\mathrm{s}\|},\boldsymbol{\beta}\right\rangle - \cos(\phi), \tag{8}$$

i.e., $g(\mathbf{x}) = 0$ for any $\mathbf{x}$ on the cone surface. Points that lie inside the cone have $g(\mathbf{x}) < 0$, and points that lie outside the cone have $g(\mathbf{x}) > 0$. Because of the continuity of the cone surface, if there are some points in voxel V_j that are inside the cone and some points in V_j that lie outside the cone, then the cone surface must pass through V_j.

We now develop a simple test based on the voxel corners, as illustrated in two dimensions in Fig. 2. For voxel V_j with center $\mathbf{v}_j$, we define the set of 8 voxel corner points $\{\mathbf{w}_j^{(k)}\}_{k=1}^8$, where the positions are given as $\mathbf{w}_j^{(k)} = \mathbf{v}_j + (\pm d_x/2, \pm d_y/2, \pm d_z/2)$ for voxels with dimensions $d_x \times d_y \times d_z$. If there exist corner indices $m, n \in \{1,\dots,8\}$ such that $g(\mathbf{w}_j^{(m)}) < 0$ and $g(\mathbf{w}_j^{(n)}) > 0$, then the cone surface must pass through V_j, and $\mathbb{I}_{\mathrm{cone}}(V_j) = 1$. Otherwise, we set $\mathbb{I}_{\mathrm{cone}}(V_j) = 0$, which is true with high probability. It is possible for the cone surface to intersect the edge of a voxel despite all 8 corners lying outside the cone as shown in the top view in Fig. 2b; however, we consider this probability to be negligible, especially for small voxels and large cone radii.

3) Proposed system matrix accounting for spatial ambiguity: Due to the limitation of spatial resolution of the detector arrays, when a pair of scatterer index and absorber index is recorded, there is an ambiguity of the location where the photon hits the scatterer and absorber within those detector pixels. In other words, a measurement does not determine a cone, but a region surrounding the cone. Ignoring this ambiguity can lead to unreliable reconstruction, especially when the number of measurements is small and when the source is situated far from the detector. In our work, we assume the energy recordings are sufficiently accurate and ignore the half-angle ambiguity, thus $p_{\phi|\tilde{\phi}}(\phi|\tilde{\phi}) = \delta(\phi-\tilde{\phi})$. We ignore the thickness of the detector and model the detector pixel as the largest disc contained in that pixel whose radius is denoted by r_{pix}. That is, we define $p(\mathbf{r}_\mathrm{s}|\tilde{\mathbf{r}}_\mathrm{s})$ as uniform for $\tilde{\mathbf{r}}_\mathrm{s}$ in the disc centered at $\mathbf{r}_\mathrm{s}$, and a similar definition is applied to $p(\mathbf{r}_\mathrm{a}|\tilde{\mathbf{r}}_\mathrm{a})$.

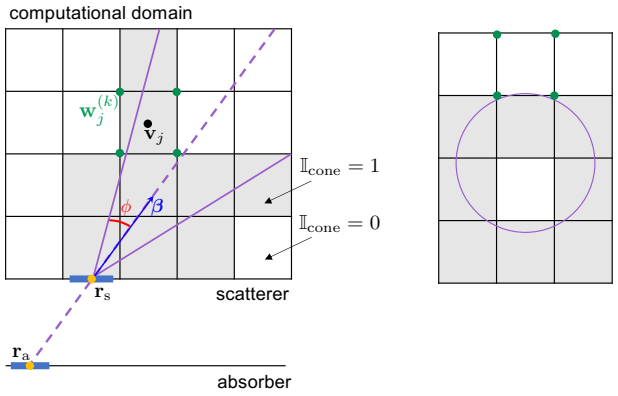

(a) side view (b) top view

Fig. 2: (a) The cone indicator function can be determined by testing whether all voxel corners lie inside or outside the cone surface. (b) The top view also shows a possible missed case that is highly unlikely to occur.

$$\mathbf{T}_{i,j} = \frac{K(\phi^{(i)}|E_\gamma)}{\mathrm{vol}(V_j)}\int_{V_j}\int_{\mathrm{disc}(\mathbf{r}_\mathrm{s}^{(i)},r_{\mathrm{pix}})}\left\{\frac{|\cos[\angle(\mathbf{x}-\tilde{\mathbf{r}}_\mathrm{s}')]|}{\|\mathbf{x}-\tilde{\mathbf{r}}_\mathrm{s}'\|_2^2} \int_{\mathrm{disc}(\mathbf{r}_\mathrm{a}^{(i)},r_{\mathrm{pix}})}\frac{|\cos[\angle(\tilde{\mathbf{r}}_\mathrm{a}'-\tilde{\mathbf{r}}_\mathrm{s}')]|}{\|\tilde{\mathbf{r}}_\mathrm{a}'-\tilde{\mathbf{r}}_\mathrm{s}'\|_2^2} \delta(\phi^{(i)}-\phi(\mathbf{v}_j;\tilde{\mathbf{r}}_\mathrm{a}',\tilde{\mathbf{r}}_\mathrm{s}'))\right\}\mathrm{d}\tilde{\mathbf{r}}_\mathrm{a}'\mathrm{d}\tilde{\mathbf{r}}_\mathrm{s}'\,\mathrm{d}\mathbf{x}\,, \tag{9}$$

where $\mathrm{disc}(\mathbf{c}, r)$ denotes the disc centered at $\mathbf{c}$ and with radius r. Finally, we use the center $\mathbf{v}_j$ to represent the voxel V_j and evaluate whether it lies in the ambiguity region. Therefore, our proposed system matrix accounting for spatial ambiguity is a special case of (3) and can be written as

$$\mathbf{T}_{i,j}^{\mathrm{amb}} \propto K(\phi^{(i)}|E_\gamma)\frac{|\cos[\angle(\mathbf{v}_j-\tilde{\mathbf{r}}_\mathrm{s}')]|}{\|\mathbf{v}_j-\tilde{\mathbf{r}}_\mathrm{s}'\|_2^2} \frac{|\cos[\angle(\tilde{\mathbf{r}}_\mathrm{a}'-\tilde{\mathbf{r}}_\mathrm{s}')]|}{\|\tilde{\mathbf{r}}_\mathrm{a}'-\tilde{\mathbf{r}}_\mathrm{s}'\|_2^2}\mathbb{I}_{\mathrm{amb}}(\mathbf{v}_j;\mathbf{r}_\mathrm{a}^{(i)},\mathbf{r}_\mathrm{s}^{(i)},\phi^{(i)}), \tag{10}$$

where

$$\mathbb{I}_{\mathrm{amb}}(\mathbf{v}_j;\mathbf{r}_\mathrm{a}^{(i)},\mathbf{r}_\mathrm{s}^{(i)},\phi^{(i)}) = \begin{cases} 1, & \mathbf{v}_j \text{ in ambiguity region} \\ 0, & \text{otherwise.} \end{cases} \tag{11}$$

In the following, we discuss how to approximate the indicator function $\mathbb{I}_{\mathrm{amb}}(\mathbf{v}_j)$.

III. Approximated Spatial Ambiguity Model

In this section, we introduce an approximation to the ambiguity region. Our goal is to have a model that is sufficiently accurate for reliable reconstruction and the representation is simple enough for efficiently building the forward operator. A graphic illustration of our model is shown in Figure 3.

A. Cone Axis Ambiguity

Given a measurement tuple $(\mathbf{r}_\mathrm{s}, \mathbf{r}_\mathrm{a}, \phi)$, the cone axis direction can be from any point within $\mathrm{disc}(\mathbf{r}_\mathrm{a}, r_\mathrm{pix})$ on the absorber to any point within $\mathrm{disc}(\mathbf{r}_\mathrm{s}, r_\mathrm{pix})$ on the scatterer. At any z-plane in the computational domain, the intersection of complete set of cone axes with the z-plane also forms a disc, corresponding to the cone axis ambiguity at that distance. Denote the positions of the centers of the current pixels on scatterer and absorber by $\mathbf{r}_\mathrm{s} = (x_s, y_s, z_s)$ and $\mathbf{r}_\mathrm{a} = (x_a, y_a, z_a)$, respectively. At a z-plane, the cone axis ambiguity disc has center $\mathbf{p}_0 = (x_0, y_0, z)$ and radius r_z given by

$$\begin{aligned} x_0 &= x_s + \frac{z - z_s}{z_s - z_a}(x_s - x_a) \\ y_0 &= y_s + \frac{z - z_s}{z_s - z_a}(y_s - y_a), \\ r_z &= \frac{z - (z_s + z_a)/2}{(z_s + z_a)/2 - z_a} r_\mathrm{pix}. \end{aligned} \tag{12}$$

The boundary of the cone axis ambiguity disc is the circle on the z-plane that can be parameterized by $\theta \in [0, 2\pi)$ as

$$x_\mathrm{c}(\theta) = x_0 + r_z \cos(\theta), \quad y_\mathrm{c}(\theta) = y_0 + r_z \sin(\theta). \tag{13}$$

For a fixed boundary point $\mathbf{p}_\mathrm{c}(\theta) = (x_\mathrm{c}(\theta), y_\mathrm{c}(\theta), z)$, we can trace back to find the corresponding cone vertex $\mathbf{v}(\theta)$ on the scatterer and the cone axis direction $\boldsymbol{\beta}(\theta)$, which along with an angle ϕ fully expresses the cone.

B. Source Ambiguity Region

We next describe how the ambiguity in the cone axis affects the possible locations of a radiation source, given an angle measurement ϕ. We focus on the possible source locations for the most extreme cone axis positions, which lie on the boundary of the disc, and thus define the boundary of the source ambiguity region. In fact, these cones define both an exterior and interior boundary, which we fit with ellipses or hyperbolas, although in some cases, only the exterior boundary will be used.

1) Boundary Points: To find the approximate interior and exterior boundaries of the ambiguity region, we define points $\mathbf{p}_\mathrm{i}(\theta) = (x_\mathrm{i}(\theta), y_\mathrm{i}(\theta), z)$ and $\mathbf{p}_\mathrm{e}(\theta) = (x_\mathrm{e}(\theta), y_\mathrm{e}(\theta), z)$ for each point $\mathbf{p}_\mathrm{c}(\theta)$ on the disc boundary; see the red cone in Fig. 3b. These points are defined by two constraints: 1) they are on the line connecting $\mathbf{p}_0$ and $\mathbf{p}_\mathrm{c}$ and 2) the angle between $\mathbf{v}(\theta) + \boldsymbol{\beta}(\theta)$ and either $\mathbf{p}_\mathrm{i}(\theta)$ or $\mathbf{p}_\mathrm{e}(\theta)$ is ϕ. To distinguish the interior and exterior points, we define $\mathbf{p}_\mathrm{i}(\theta)$ to be on the ray from $\mathbf{p}_\mathrm{c}(\theta)$ toward $\mathbf{p}_0(\theta)$, whereas $\mathbf{p}_\mathrm{e}(\theta)$ is on the ray from $\mathbf{p}_0(\theta)$ toward $\mathbf{p}_\mathrm{c}(\theta)$. Mathematically,

$$\langle \mathbf{p}_\mathrm{i}(\theta) - \mathbf{p}_\mathrm{c}(\theta), \mathbf{p}_\mathrm{c}(\theta) - \mathbf{p}_0(\theta) \rangle < 0 \tag{14}$$

$$\langle \mathbf{p}_\mathrm{e}(\theta) - \mathbf{p}_\mathrm{c}(\theta), \mathbf{p}_\mathrm{c}(\theta) - \mathbf{p}_0(\theta) \rangle > 0, \tag{15}$$

where $\langle \cdot \rangle$ denotes the inner product. For each point $\mathbf{p}_\mathrm{e}(\theta)$ and $\mathbf{p}_\mathrm{i}(\theta)$, we solve for coordinates (x, y) such that

$$y - y_0 = \frac{y_c(\theta) - y_0}{x_c(\theta) - x_0}(x - x_0) \tag{16}$$

$$\cos(\phi) = \left\langle \frac{\mathbf{v}(\theta) + \boldsymbol{\beta}(\theta)}{\|\mathbf{v}(\theta) + \boldsymbol{\beta}(\theta)\|}, \frac{(x, y, z)}{\|(x, y, z)\|} \right\rangle. \tag{17}$$

In cases where the cone axis is less tilted and/or the cone angle is sufficiently small, we obtain solutions for both $\mathbf{p}_\mathrm{e}(\theta)$ and $\mathbf{p}_\mathrm{i}(\theta)$, whereas in other cases, we only obtain a solution only for $\mathbf{p}_\mathrm{i}(\theta)$.

2) Solid Ellipse vs Ring Regions: We repeat the same calculation for $\mathbf{p}_\mathrm{e}(\theta + \pi)$ and $\mathbf{p}_\mathrm{i}(\theta + \pi)$ associated with $\mathbf{p}_\mathrm{c}(\theta + \pi)$ (the yellow cone in Fig. 3b). Suppose that we obtained two solutions for both cones as shown on the bottom right in Fig. 3b. If the two points of the yellow cone and the two points of the red cone do not interlace (e.g., for a small cone angle), then all of the points inside the exterior boundary are possible locations for the radiation source. This implies a solid ambiguity region, in this case an ellipse, so the interior boundary is discarded. If the points for the θ and $\theta + \pi$ cones do interlace (e.g., for large cone angle), then there is an open portion in the interior of the ambiguity region whose points do not lie on any plausible Compton cone surface. We then call the ambiguity region a "ring," which has both interior and exterior boundaries. As we sweep θ from 0 to π, the indication of solid ellipse or ring determined by the cones at θ and $\theta + \pi$ may be mixed, in which case, we approximate it as a solid ellipse.

3) Fitting Ellipses or Hyperbolas: We observed that the collection of points $\mathcal{X}_\mathrm{i} = \{(x_\mathrm{i}(\theta), y_\mathrm{i}(\theta), z) : \theta \in [0, 2\pi)\}$ can be approximated by an ellipse when there are two solutions for all θ, whereas when there is only one solution for θ in a continuous interval in $[0, 2\pi)$, it can be approximated as a hyperbola; we call this the interior shell of the ambiguity region. Similarly, $\mathcal{X}_\mathrm{e} = \{(x_\mathrm{e}(\theta), y_\mathrm{e}(\theta), z) : \theta \in [0, 2\pi)\}$ defines the exterior shell. Therefore, we can obtain the parameters for ellipse or hyperbola for the interior (resp. exterior) shell by least squares fit to the points $\mathcal{X}_\mathrm{i}$ (resp. $\mathcal{X}_\mathrm{e}$) computed from a discrete set of θ angles. We used 100 equally spaced θ values in $[0, 2\pi)$ for the simulation results presented in Section V. Specifically, we first fit a conic section

$$Ax^2 + Bxy + Cy^2 + Dx + Ey + 1 = 0. \tag{18}$$

If $B^2 - 4AC < 0$, it is a shifted and rotated ellipse:

$$\begin{aligned} f_\text{ellipse}(x, y) = &\frac{\left[(x - c_x)\cos(\alpha) + (y - c_y)\sin(\alpha)\right]^2}{a^2} \\ &+ \frac{\left[(x - c_x)\sin(\alpha) - (y - c_y)\cos(\alpha)\right]^2}{b^2} = 1. \end{aligned}$$

If $B^2 - 4AC > 0$, it is a shifted and rotated hyperbola:

$$\begin{aligned} f_\text{hyperbola}(x, y) = &\frac{\left[(x - c_x)\cos(\alpha) + (y - c_y)\sin(\alpha)\right]^2}{a^2} \\ &- \frac{\left[(x - c_x)\sin(\alpha) - (y - c_y)\cos(\alpha)\right]^2}{b^2} = 1. \end{aligned}$$

We can then relate the center (c_x, c_y), clock-wise rotation angle α, major axis radius a, and minor axis radius b to the

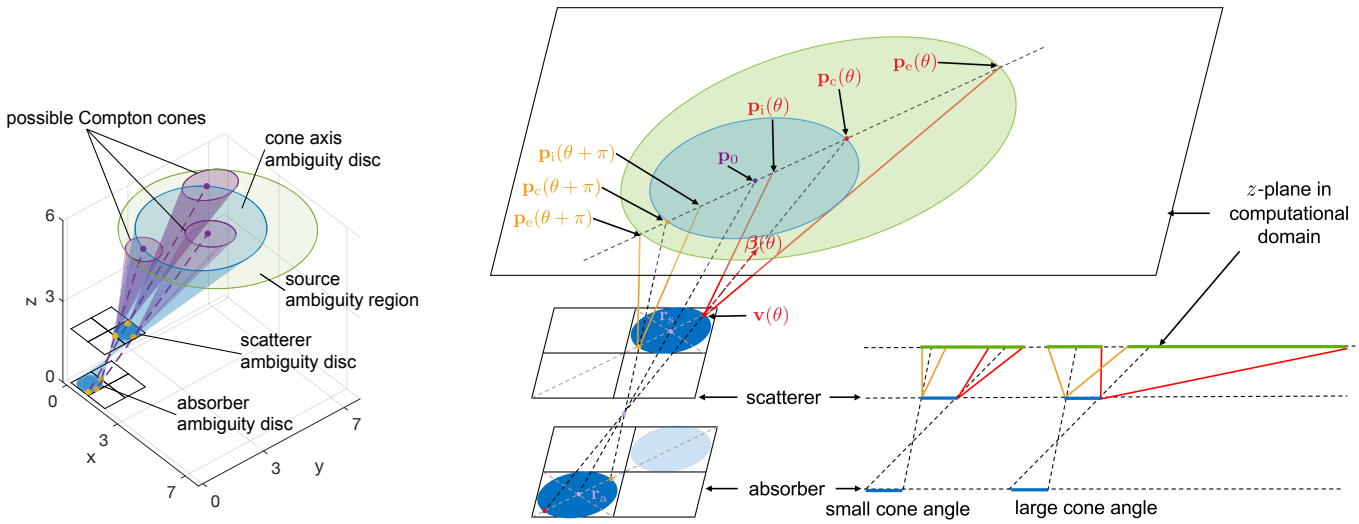

(a) (b)

Fig. 3: Illustration of spatial ambiguity in the computational domain due to limited spatial resolution of the detector arrays. (a) Detector pixels are approximated by discs. The resulting possible Compton cones (purple) have axes whose intersection with any z-plane is a cone axis ambiguity disc (blue). Depending on the angle ϕ, the set of possible Compton cones traces out a larger region (green) corresponding to the ambiguity in the radiation source position. (b) To fit the source ambiguity region with a conic section, we solve for interior and exterior boundary points. If there are two intersections for both cones (red and yellow), the ambiguity region boundary is approximated as an ellipse; else if only one solution exists, the region boundary is approximated by a hyperbola. The interior intersections determine whether the ambiguity region is solid or an open ring.

estimated parameters (A, B, C, D, E). Specifically, for both ellipse and hyperbola,

$$c_x = \frac{2CD - BE}{B^2 - 4AC}, \quad c_y = \frac{2AE - BD}{B^2 - 4AC}$$
$$\alpha = \frac{1}{2}\arctan\left(\frac{B}{A - C}\right).$$

Let

$$F = Ac_x^2 + Bc_xc_y + Cc_y^2 - 1, \tag{19}$$

then we have

$$a^2 = \frac{F\cos(2\alpha)}{A\cos^2(\alpha) - C\sin^2(\alpha)}, \quad b^2 = \frac{\pm F\cos(2\alpha)}{C\cos^2(\alpha) - A\sin^2(\alpha)},$$

where in the expression for b^2, the '+' sign is for ellipse, whereas the '−' sign is for hyperbola. Note that a hyperbola has two branches and they lie in two different half-spaces separated by the line perpendicular to the major axis and passing through the center (c_x, c_y). The branch that we are interested in is the one in the half-space whose normal and the vector $(x_s - x_a, y_s - y_a)$ form an angle less than $90°$. Fig. 4 shows an example for the least squares fit results.

Once the parameters for the ellipse or hyperbola have been determined, it is convenient to test whether an arbitrary point $\mathbf{v}_j$ in the computation domain is in the ambiguity region, and thus whether $\mathbb{I}_{\text{amb}}(\mathbf{v}_j)$ equals 0 or 1. For example, consider the $\mathbf{v}_j = (x_j, y_j, z)$'s on a z-plane, if the ambiguity region is between two hyperbola as in the first plot in Fig. 4, then $\mathbb{I}_{\text{amb}}(\mathbf{v}_j) = 1$ if the following conditions are satisfied:

$$f^{\text{i}}_{\text{hyperbola}}(x_j, y_j) \le 1, \quad f^{\text{e}}_{\text{hyperbola}}(x_j, y_j) \ge 1,$$
$$\langle (x_j - c_x, y_j - c_y), (x_s - x_a, y_s - y_a)\rangle \ge 0,$$

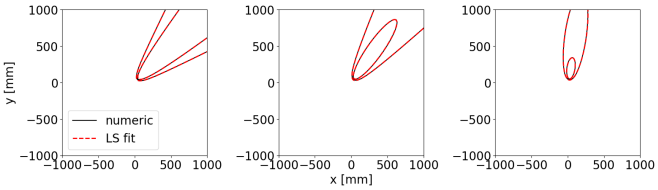

Fig. 4: Least squares fit for hyperbola and ellipse. The black solid lines represent $\mathcal{X}_\text{i}$ and $\mathcal{X}_\text{e}$, whereas the red dashed lines represent the ellipse or hyperbola obtained by least squares fit.

where $f^{\text{i}}_{\text{hyperbola}}$ and $f^{\text{e}}_{\text{hyperbola}}$ denotes the hyperbola fitted by $\mathcal{X}_\text{i}$ and $\mathcal{X}_\text{e}$, respectively. As another example, if the ambiguity region is between an ellipse and a hyperbola as in the second plot in Fig. 4, then $\mathbb{I}_{\text{amb}}(\mathbf{v}_j) = 1$ if the following conditions are satisfied:

$$f^{\text{i}}_{\text{ellipse}}(x_j, y_j) \ge 1, \quad f^{\text{e}}_{\text{hyperbola}}(x_j, y_j) \ge 1,$$
$$\langle (x_j - c_x, y_j - c_y), (x_s - x_a, y_s - y_a)\rangle \ge 0.$$

Other cases can be defined in a similar way.

An example for the ambiguity region with various scatterer-absorber locations is shown in Fig. 5. We notice that a solid ellipse is obtained at the bottom-left plot in Fig. 5a. This is the case when the cone angle is comparatively small and the scatterer pixel is directly above the absorber pixel, thus the cone axes are not so tilted throughout the ambiguity region. The other extreme is shown at the top-right plot in Fig. 5b, where we obtained a region in between two hyperbolas. This is the case when the cone angle is comparatively large and the scatterer pixel is horizontally farther away from the absorber

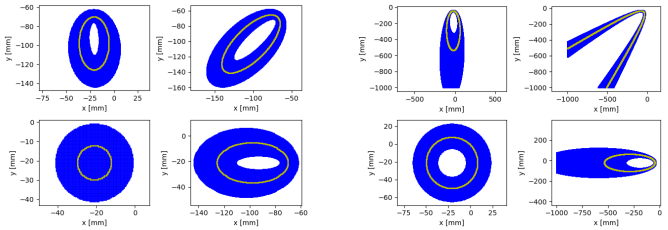

(a) Cone angle $\phi = 10^\circ$. (b) Cone angle $\phi = 30^\circ$.

Fig. 5: Cone surfaces (yellow) and ambiguity regions (blue) surrounding them at the plane $z = 50$ mm. Both scatterer and absorber have 8×8 detection elements and the distance between scatterer and absorber is 30 mm. The size of each element is 5×5 mm (i.e., $r_{\text{pix}} = 2.5$ mm) and there is a 1 mm gap between neighboring elements. The scatterer position is fixed at the bottom-left corner and the absorber locations vary over the four corners of an 8×8 array.

pixel, thus the cone axes are very tilted. Additional cases between these two extremes are shown in the rest of the plots in Fig. 5, where the ambiguity region is a ring between two ellipses.

IV. Inverse Problem

A. Measurement Selection

Although the modeling assumes a perfect event is recorded other than the spatial ambiguity, with Compton scattering and photon absorption happening at a single pixel in each of the respective detectors, actual Compton camera measurements themselves are highly ambiguous. One major challenge is that the sequence of photon hits cannot usually be tracked, so there are often multiple plausible sequences (e.g., Compton scattering occurs at the absorber, and the photon is back-scattered and absorbed by the scatterer) that result in dramatically different cones [18], [19]. Other ambiguities arise if the energy from an interaction is deposited in multiple pixels of the same detector, or if the energy is incompletely deposited, so that $E_{\text{s}} + E_{\text{a}} \neq E_\gamma$. To avoid modelling all of these additional ambiguities, we follow convention in selecting only events that meet the following criteria, based on assumptions of a ^{137}Cs radiation source (with characteristic emission of 662-keV gamma photons) and Cesium Iodide (CsI) detectors:

1) **Total energy:** the gamma photons used in our simulation have energy $E_\gamma = 0.662$ MeV, and we only use measurements with $E_s + E_a > 0.66$ MeV.
2) **Excluding fluorescence X-ray contamination:** for CsI detectors, X-rays with energy approximately 0.045 MeV escape from the absorber and are then absorbed by the scatterer [20, pp. 472]. This has nothing to do with Compton scattering and the angle of the X-ray is completely random. We observed in our simulation that the measurements with $E_s \in [0.025, 0.045]$ MeV are likely due to X-ray contamination and we exclude them for reconstruction.

B. Sequencing

For the recorded events satisfying the above criteria, we observed that with our configuration of the Compton camera, the number of back-scattering events (i.e., the photon hits the absorber first and then is back-scattered to the scatterer, thus the role of the scatterer and the absorber is interchanged) is non-negligible. Therefore, we include the following sequencing techniques in our method for more reliable reconstruction:
1) **Compton edge test:** for a given event, if the recorded energy is greater than the Compton edge energy, which is defined as

$$E_{\text{edge}} = E_\gamma \left(1 - \frac{1}{1 + \frac{2E_\gamma}{m_e c^2}}\right), \tag{20}$$

then this cannot be the first interaction, because this is the largest possible energy deposited during Compton scattering.
2) **Probabilistic combination:** when both recorded energies pass the Compton edge test, either of them can be the first interaction. It has been shown [21] that the (non-normalized) probability of (E_1, ϕ) being the first hit can be computed as

$$K(\phi; E_\gamma) \frac{2\pi m_e c^2}{(E_\gamma - E_1)^2} \frac{1}{2\pi \sin(\phi)}, \tag{21}$$

where $K(\phi; E_\gamma)$ denotes the Klein-Nishina formula. However, in our experiments, the sequence determined directly by this probability does not seem to be very accurate. We observed that a large number of events that are supposed to be forward scattering have higher probability of being back scattering. We found that an ad-hoc correction by scaling the back-scattering probability by 0.6 seems to result in more reasonable sequences. Therefore, in all our simulations, we apply this ad-hoc modification to the probability.

C. List-Mode Maximum Likelihood Expectation Maximization

With some initial estimate of the source intensity distribution $\lambda^{(0)}$, the algorithm proceeds as

$$\boldsymbol{\lambda}^{(t+1)} = \frac{\boldsymbol{\lambda}^{(t)}}{s} \odot \left(\mathbf{T}^{\mathsf{T}} \frac{\mathbf{1}}{\mathbf{T}\boldsymbol{\lambda}^{(t)}}\right), \tag{22}$$

where $\odot$ denotes coordinate-wise multiplication and the divisions are all coordinate-wise.

V. Simulation Results

We now test our reconstruction method on Geant4 simulated data. A single point source with energy 0.662 MeV is utilized. Both the scatterer and the absorber have 8×8 pixels made of Cesium Iodide (CsI) and of size $5 \times 5 \times 5$ mm^3. There is a 1 mm gap between pixels. The scatterer is placed at depth $z = 0$ mm and the absorber is placed at depth $z = -30$ mm.

In the first set of simulations, we fix the source location at $(20, 20, 50)$ mm and vary the number of measurements. We select measurements that satisfy the criteria in Section IV-A as well as $E_s < E_{\text{edge}}$. All these measurements are treated as forward scattering events. The computational domain is a $64 \times 64 \times 33$ volume and the physical size of the volume is shown in the figures. We can see from Fig. 6a and Fig. 6b that by using our ambiguity model instead of the cone surface

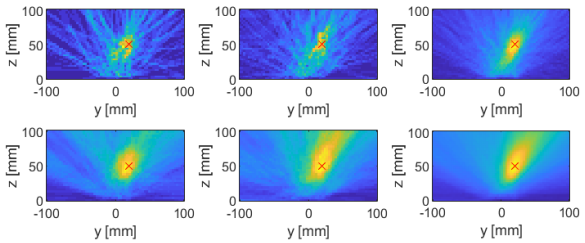

(a) Back-projection

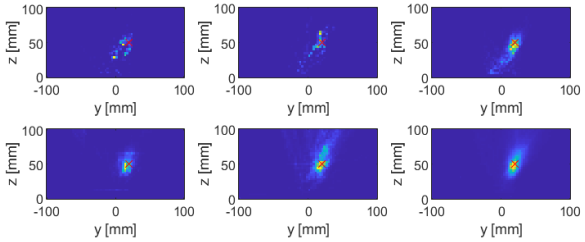

(b) LM-MLEM

Fig. 6: Reconstruction of the yz-slice at the true x position. First row: cone surface model. Second row: ambiguity region model. From left to right: the number of measurements is 64, 132, 1375, respectively. The red cross shows the true source position.

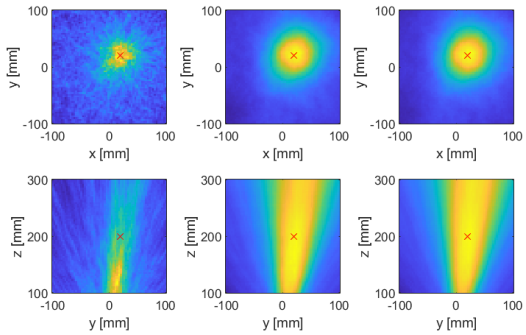

(a) Back-projection

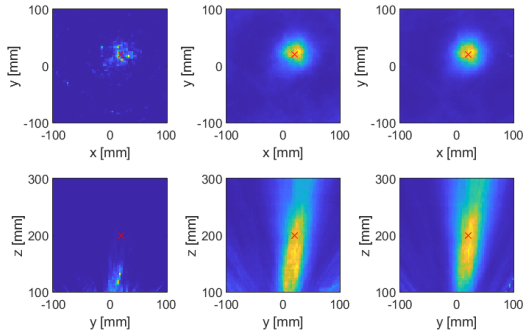

(b) LM-MLEM

Fig. 7: Reconstruction of the xy-slice at the true z position (top row) the yz-slice at the true x position (bottom row). First and second columns: cone surface model and ambiguity region model, respectively, with all selected measurements treated as forward scattering after Compton edge test for E_s. Third column: ambiguity region model with probabilistic combination of forward- and back-scattering events.

model in the forward operator, we are able to obtain higher quality reconstruction with the same number of measurements. Alternatively, we can achieve good source distribution reconstructions with a smaller number of detected photons.

In the second set of simulation, we move the source farther away from the detector and set it at $(20, 20, 200)$ mm. The computational domain is a $64 \times 64 \times 64$ volume and the physical size of the volume is shown in the figures. As we can see from the first column in Fig. 7a and Fig. 7b, the cone surface model results in a significant bias towards the detector along the z-direction. Comparing the second and the third columns, we notice that the error due to back-scattering is non-negligible along the z-direction and a probabilistic combination of forward- and back-scattering events yields more accurate reconstruction when the source is far from the detector.

VI. Conclusion

We have demonstrated that accounting for ambiguities due to the spatial resolution of a Compton camera can improve source distribution reconstruction, enabling the use of a smaller number of detected photons. Our ambiguity model is based on an approximation of the detector pixels by a disc, and then approximating the resulting ambiguity regions as being bounded by conic sections for a given depth plane. Future work may use more accurate models that also take the pixel depth into account, as well as investigating the combination of ambiguity models for both spatial and energy resolution.

References

[1] A. H. Compton, "A quantum theory of the scattering of X-rays by light elements," *Physical Review*, vol. 21, no. 5, pp. 483–502, May 1923.

[2] S. Wilderman, N. Clinthorne, J. Fessler, and W. Rogers, "List-mode maximum likelihood reconstruction of Compton scatter camera images in nuclear medicine," in *IEEE Nuclear Science Symposium and Medical Imaging Conference*, Nov. 1998, vol. 3, pp. 1716–1720 vol.3.

[3] S. Wilderman, J. Fessler, N. Clinthorne, J. LeBlanc, and W. Rogers, "Improved modeling of system response in list mode EM reconstruction of Compton scatter camera images," *IEEE Transactions on Nuclear Science*, vol. 48, no. 1, pp. 111–116, Feb. 2001.

[4] S. R. Tornga, M. W. Rawool Sullivan, and J. P. Sullivan, "Three-dimensional Compton imaging using list-mode maximum likelihood expectation maximization," *IEEE Transactions on Nuclear Science*, vol. 56, no. 3, pp. 1372–1376, June 2009.

[5] V. Maxim, M. Frandeş, and R. Prost, "Analytical inversion of the Compton transform using the full set of available projections," *Inverse Problems*, vol. 25, no. 9, pp. 095001, Aug. 2009.

[6] V. Maxim, "Filtered backprojection reconstruction and redundancy in Compton camera imaging," *IEEE Transactions on Image Processing*, vol. 23, no. 1, pp. 332–341, Jan. 2014.

[7] V. Maxim, X. Lojacono, E. Hilaire, J. Krimmer, E. Testa, D. Dauvergne, I. Magnin, and R. Prost, "Probabilistic models and numerical calculation of system matrix and sensitivity in list-mode MLEM 3D reconstruction of Compton camera images," *Physics in Medicine and Biology*, vol. 61, no. 1, pp. 243–264, Dec. 2016.

[8] F. Terzioglu, P. Kuchment, and L. Kunyansky, "Compton camera imaging and the cone transform: a brief overview," *Inverse Problems*, vol. 34, no. 5, pp. 054002, May 2018.

[9] F. Terzioglu, "Exact inversion of an integral transform arising in Compton camera imaging," *Journal of Medical Imaging*, vol. 7, no. 3, pp. 032504, Mar. 2020.

[10] C. J. Solomon and R. J. Ott, "Gamma ray imaging with silicon detectors — A Compton camera for radionuclide imaging in medicine," *Nuclear*

Instruments and Methods in Physics Research Section A: Accelerators, Spectrometers, Detectors and Associated Equipment, vol. 273, no. 2-3, pp. 787–792, Dec. 1988.

[11] A. Hoover, R. Kippen, J. Sullivan, M. Rawool-Sullivan, W. Baird, and E. Sorensen, "The LANL prototype Compton gamma-ray imager: design and image reconstruction techniques," *IEEE Transactions on Nuclear Science*, vol. 52, no. 6, pp. 3047–3053, Dec. 2005.

[12] I. Tsitsimpelis, C. J. Taylor, B. Lennox, and M. J. Joyce, "A review of ground-based robotic systems for the characterization of nuclear environments," *Progress in Nuclear Energy*, vol. 111, pp. 109–124, Mar. 2019.

[13] B. D. Milbrath, A. J. Peurrung, M. Bliss, and W. J. Weber, "Radiation detector materials: An overview," *Journal of Materials Research*, vol. 23, no. 10, pp. 2561–2581, Oct. 2008.

[14] M. Hirasawa and T. Tomitani, "An analytical image reconstruction algorithm to compensate for scattering angle broadening in Compton cameras," *Physics in Medicine and Biology*, vol. 48, no. 8, pp. 1009–1026, Apr. 2003.

[15] D. Xu and Z. He, "Gamma-ray energy-imaging integrated spectral deconvolution," *Nuclear Instruments and Methods in Physics Research Section A: Accelerators, Spectrometers, Detectors and Associated Equipment*, vol. 574, no. 1, pp. 98–109, Apr. 2007.

[16] L. Parra and H. Barrett, "List-mode likelihood: EM algorithm and image quality estimation demonstrated on 2-D PET," *IEEE Transactions on Medical Imaging*, vol. 17, no. 2, pp. 228–235, Apr. 1998.

[17] O. Klein and Y. Nishina, "The scattering of light by free electrons according to Dirac's new relativistic dynamics," *Nature*, vol. 122, no. 3072, pp. 398–399, Sept. 1928.

[18] A. C. Zoglauer, *First Light for the Next Generation of Compton and Pair Telescopes*, Ph.D. thesis, Technische Universität München, 2005.

[19] C. Wahl, *Imaging, Detection, and Identification Algorithms for Position-Sensitive Gamma-Ray Detectors*, Ph.D. thesis, University of Michigan, 2011.

[20] D. Aitken, B. Beron, G. Yenicay, and H. Zulliger, "The fluorescent response of NaI (Tl), CsI (Tl), CsI (Na) and CaF_2 (Eu) to X-rays and low energy gamma rays," *IEEE Transactions on Nuclear Science*, vol. 14, no. 1, pp. 468–477, 1967.

[21] D. Xu, Z. He, C. E. Lehner, and F. Zhang, "4-pi Compton imaging with single 3D position-sensitive CdZnTe detector," in *Hard X-Ray and Gamma-Ray Detector Physics VI*. International Society for Optics and Photonics, 2004, vol. 5540, pp. 144–155.